A LETTERS JOURNAL EXPLORING THE FRONTIERS OF PHYSICS

Società Italiana di Fisica

sciences IOP Institute of Physics

LETTER

Comparison of cryogenic (hydrogen) and TESPEL (polystyrene) pellet particle deposition in a magnetically confined plasma

To cite this article: K. J. McCarthy *et al* 2017 *EPL* **120** 25001

View the article online for updates and enhancements.

You may also like

- Improvements in a Tracer-Encapsulated Solid Pellet and Its Injector for More Advanced Plasma Diagnostics
Naoki Tamura, Shigeru Sudo, Chihiro Suzuki et al.
- Development of a double-barreled Tracer Encapsulated Solid Pellet (TESPEL) injection system for LHD
N. Tamura, H. Hayashi, N. Uejima et al.
- A review of impurity transport characteristics in the LHD
Shigeru Sudo

This content was downloaded from IP address 18.117.142.128 on 25/04/2024 at 17:26

A Letters Journal Exploring the Frontiers of Physics

October 2017

EPL, **120** (2017) 25001
doi: 10.1209/0295-5075/120/25001

www.epljournal.org

Comparison of cryogenic (hydrogen) and TESPEL (polystyrene) pellet particle deposition in a magnetically confined plasma

K. J. McCarthy[1(a)], N. Tamura[2], S. K. Combs[3], N. Panadero[1], E. Ascabíbar[1], T. Estrada[1], R. García[1], J. Hernández Sánchez[1], A. López Fraguas[1], M. Navarro[1], I. Pastor[1], A. Soleto[1] and TJ-II Team[1]

[1] *Laboratorio Nacional de Fusión, CIEMAT - Madrid, Spain*
[2] *National Institute for Fusion Science - Toki, Japan*
[3] *Fusion & Materials for Nuclear Systems Division, ORNL - Oak Ridge, TN, USA*

received 29 September 2017; accepted in final form 2 December 2017
published online 5 January 2018

PACS 52.55.Hc – Stellarators, torsatrons, heliacs, bumpy tori and other toroidal confinement devices
PACS 52.70.-m – Plasma diagnostic techniques and instrumentation
PACS 52.25.Vy – Impurities in plasmas

Abstract – A cryogenic pellet injector (PI) and tracer encapsulated solid pellet (TESPEL) injector system has been operated in combination on the stellarator TJ-II. This unique arrangement has been created by piggy-backing a TESPEL injector onto the backend of a pipe-gun–type PI. The combined injector provides a powerful new tool for comparing ablation and penetration of polystyrene TESPEL pellets and solid hydrogen pellets, as well as for contrasting subsequent pellet particle deposition and plasma perturbation under analogous plasma conditions. For instance, a significantly larger increase in plasma line-averaged electron density, and electron content, is observed after a TESPEL pellet injection compared with an equivalent cryogenic pellet injection. Moreover, for these injections from the low-magnetic-field side of the plasma cross-section, TESPEL pellets deposit electrons deeper into the plasma core than cryogenic pellets. Finally, the physics behind these observations and possible implications for pellet injection studies are discussed.

Copyright © EPLA, 2018

Introduction. – Cryogenic pellet injection is a widely used fuelling technique for many medium- and large-sized magnetically confined plasma devices [1,2]. The idea was first proposed in 1954 [3] as a means for transporting fuel across the confining magnetic fields to the plasma core. Over the last few decades the technology has become mature and cryogenic pellet injection is now the prime candidate for core fuelling of the ITER reactor [4]. In the intervening time, the injection of solid, non-cryogenic, pellets has been used as a method to study impurity transport, among other topics [5,6]. One such technique is the tracer encapsulated solid pellet (TESPEL) method [7]. It involves injecting a tracer-loaded polystyrene capsule so that the impurity element it contains is deposited directly in the plasma core, thereby eliminating inward diffusion from the physics [8]. Although the *raison d'être* of these injection methods is distinct, both types should undergo the same, or similar, physical processes along their flight paths towards the plasma centre. Subsequently, particles in the partially ionized cloud that surrounds an ablating pellet should experience the same physical force(s) hence they should undergo similar drift and diffusion processes. However, to the authors' knowledge, there is no systematic comparison of both processes. One reason is the limited number of devices equipped with both cryogenic and impurity pellet injection systems [9–11]. Even if both are available, they tend to have different injection geometries or to be located in different machine sectors. In the stellarator TJ-II [12], a TESPEL injector was recently piggy-backed onto the backend of a pipe-gun–type cryogenic pellet injector [13]. This makes it unique as both pellet types can be injected along adjoining guide tubes into the same toroidal sector of this stellarator, albeit not simultaneously, from the low-field side (LFS) of the magnetic axis. Moreover, the same local plasma diagnostics can be used to evaluate ablation and penetration depth whilst other diagnostics provide information on plasma perturbation as well as pellet particle transport and deposition [14]. In order to facilitate comparison studies, cryogenic and TESPEL pellets with similar penetration

(a) E-mail: kieran.mccarthy@ciemat.es

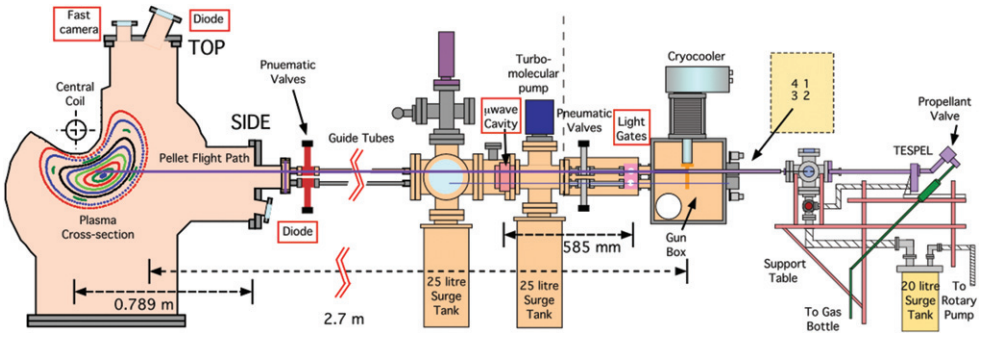

Fig. 1: (Colour online) Sketch of the cross-section of the TJ-II and the cryogenic pellet injector with the TESPEL piggy-backed onto its upstream end of *Line*-4. Pellets accelerated along a guide tube. The predicted flight path to, and through, the plasma is also indicated (the closed magnetic flux surfaces for the standard configuration are shown). The relative locations of *Lines*-1 through -4, with respect to the rear end of the PI, are highlighted.

depths are considered. The only significant technical difference is the slower TESPEL velocity, typically from 250 to 450 ms^{-1}, as compared to 800–1200 ms^{-1}. However, it is considered that its effect on, for instance, the ablation rate is minimal [15,16].

In this paper a comparative study is made of ablation, penetration depth, plasma response and particle deposition after injections of both pellet types into magnetically confined plasmas in the stellarator TJ-II. For these, pellets are injected into reproducible plasma discharges. In the first instance, the experimental penetration depth is compared for each pellet type with predictions obtained using several simple analytic formulas (scalings) developed by Sergeev *et al.* for inter-machine comparisons with a large range of pellet types [17]. These scalings consider three mechanisms that contribute to shielding, albeit to different degrees, *i.e.*, neutral gas shielding (NGS), plasma shielding and electrostatic shielding. In the second instance, a significantly higher increase in plasma line-averaged electron density after a TESPEL injection, as compared to a cryogenic pellet with a similar electron population, is reported. It is found that the fraction of deposited pellet particles is at least $\times 2$ greater for TESPEL than that for solid hydrogen. In addition, from radial density profiles, the deposited electron density profile is significantly closer to the plasma core for TESPEL. In order to understand these observations an $E \times B$ induced outward directed acceleration of the partially ionized cloud (plasmoid) that surrounds an ablating pellet is considered [2]. In particular it is discussed how these observations demonstrate experimentally the influence that pellet atom mass has on plasmoid drift as well as on pellet fuelling efficiency.

Experimental set-up. – *TJ-II stellarator.* The TJ-II is a low magnetic shear stellarator of the heliac type with a major radius of 1.5 m. Its magnetic fields are generated by a system of poloidal, toroidal and vertical field coils. The resultant cross-sections of its magnetic flux surfaces are bean shaped with a central magnetic field, B_0, ≤ 1.1 T, and average minor radius, a, of ≤ 0.22 m [12]. The plasmas considered here use hydrogen as the working gas. They are created and maintained using electron cyclotron resonance heating (ECRH) from two gyrotrons operated at 53.2 GHz, *i.e.*, the 2nd harmonic of the electron cyclotron resonance frequency (≤ 500 kW). With ECRH, central electron densities and temperatures up to $1.7 \times 10^{19}\,\mathrm{m}^{-3}$ and 1.5 keV, respectively, are achieved while the central majority ion temperature is ≤ 100 eV [18].

Cryogenic pellet injection. A pipe-gun–type cryogenic pellet injector (PI) is operating on the TJ-II [19]. It is equipped with a cryogenic refrigerator for *in situ* hydrogen pellet formation, fast propellant valves for pellet acceleration (800–1200 ms^{-1}), in-line diagnostics for determining pellet velocity and mass [20], plus straight delivery lines, called *Line*-1 to *Line*-4. See fig. 1. In this work, *Line*-1 and *Line*-4 are used since their flight paths cross the plasma centre [21]. They are equipped with a light emitting/sensitive diode combination and a shared microwave resonance cavity. The former provides a timing signal only while the latter provides a timing signal whose amplitude is mass dependent. For TJ-II, small pellets are required for experiments since the electron density must not rise above the gyrotron cut-off limit ($\sim 1.7 \times 10^{19}\,\mathrm{m}^{-3}$).

TESPEL on TJ-II. Recently, a TESPEL injector, loaned to Ciemat by the National Institute for Fusion Science in Toki, Japan, was piggy-backed onto the up-stream end of *Line*-4 [13]. For injections into ECRH plasmas on TJ-II, $\leq 320\,\mu$m diameter polystyrene polymer pellets, $(\text{-CH}(\text{C}_6\text{H}_5)\ \text{CH}_2\text{-})_\text{n}$, are used so that the post-injection central electron density is $\leq 1.7 \times 10^{19}\,\mathrm{m}^{-3}$. When undertaking impurity studies the core is drilled out and the pellet is loaded with microscopic pieces of tracer [22]. Here, unloaded complete polystyrene pellets are considered in order to avoid complications due to additional impurities. Thus, for instance, a 320 μm TESPEL pellet contains $\sim 7.9 \times 10^{17}$ H atoms (with $\sim 7.9 \times 10^{17}$ electrons) and an equal number of C atoms (with $\sim 4.74 \times 10^{18}$ electrons).

Ablation diagnostics. A significant advantage of the TJ-II PI set-up is the optical access to the pellet path through the plasma, *i.e.*, via viewports located above (TOP) and

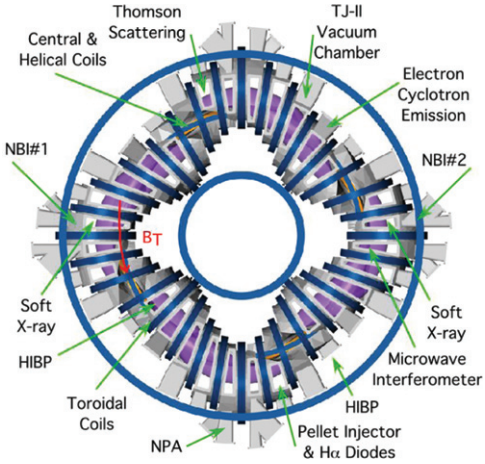

Fig. 2: (Colour online) Bird's eye view sketch of the stellarator TJ-II showing the toroidal locations of the pellet injector/TESPEL system, plus relevant diagnostics.

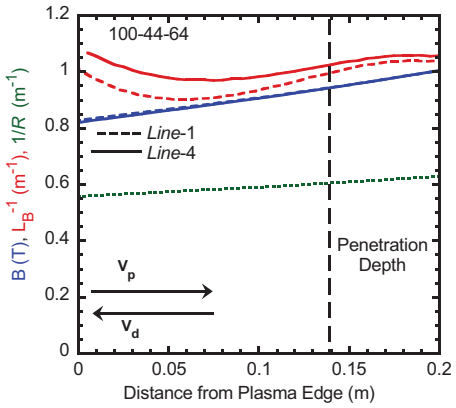

Fig. 3: (Colour online) Magnetic-field strength (T), magnetic cross-field gradient scale-length, $L_{\rm B}^{-1}$ ($\rm m^{-1}$), and inverted major radius ($\rm m^{-1}$) *vs.* distance from the outer plasma edge for flight paths of pellets injected from guide tubes *Line*-1 and *Line*-4 when using configuration 100-44-64.

behind (SIDE) the pellet flight paths. See fig. 1. In order to collect the light emitted by the neutral, or partially ionized, cloud (plasmoid) that surrounds an ablating pellet, amplified silicon diodes fitted with interference filters centred at 660 ± 2 nm, are located outside these viewports (digitized at 1 MHz). By processing this light, and knowing the pellet velocity and the pellet into plasma entry time, a Balmer H_α (at 656.3 nm) emission profile (photons per second emitted by the plasmoid) is created from which a pellet/TESPEL penetration length can be established [19]. Although it is recognized that the emission profile provides an estimate of the ablation rate, assuming that the latter is related to pellet mass loss [23], it is currently the best indicator of the ablation rate that can be made given that plasmoid temperature, density and size are not determined in TJ-II.

Plasma diagnostics. TJ-II is equipped with a wide range of plasma diagnostics [14]. Those of particular relevance here include a single laser pulse (≤ 40 ns) per discharge Thomson scattering (TS) system that provides a set of electron density and temperature profiles [24], a microwave interferometer, and a 12-channel Electron Cyclotron Emission system (the microwave-based diagnostics have 10 μs temporal resolution). The latter follow the line-integrated electron density and electron temperature evolution at different radii, respectively, and are located at 180°, 67.5°, and 123.75° toroidally, respectively, from the PI (see fig. 2). In the case of the TS, its laser chord traverses completely the plasma. However, due to viewing geometry and signal intensity considerations, profiles are limited to $\rho \leq \sim 0.8$, where ρ is normalized radius, *i.e.*, r/a.

Results. – *Experiment.* For this comparison, a $\sim$600 μm diameter solid hydrogen pellet and a 320 mm diameter TESPEL pellet are injected into plasmas created using the standard magnetic configuration with $1.56 \leq \iota/2\pi \leq 1.64$ (ι is the rotational transform), $B_0 = 0.98$ T, and a magnetic field gradient of 0.9 T/m (see fig. 3). In order to determine pellet electron deposition across the plasma minor radius, and the subsequent radial evolution with time, the shot-to-shot technique is employed. For this, pellets are injected into reproducible plasmas so that single TS measurements can be made before, during and at several instances after pellet injection. Then, estimating the initial pellet particle content from its mass (obtained with the calibrated PI microwave cavity), the percentage of pellet particles that is deposited in the plasma is determined from the increase in plasma electron content. For cryogenic pellets, the former is obtained knowing the hydrogen atom mass (1.673×10^{-27} kg), assuming that the solid hydrogen density is 88 kg/m^3 and that the pellet mass loss between the microwave cavity and the plasma edge is negligible due to the relatively short length ($\sim$1.1 m) of the straight guide tube. In this way its mass was determined to be 10.3 ± 0.5 μg from the microwave cavity signal (containing $6.2 \pm 0.3 \times 10^{18}$ hydrogen atoms and electrons). For TESPEL, the pellet particle content can be estimated assuming a polystyrene density of 1050 kg/m^3 [25]. Here, using this density value, a TESPEL pellet mass of 18.27 ± 0.3 μg (equivalent to $8 \pm 0.1 \times 10^{17}$ of both H (with $8 \pm 0.1 \times 10^{17}$ electrons) and C (with $4.81 \pm 0.08 \times 10^{18}$ electrons) atoms, providing $5.61 \pm 0.1 \times 10^{18}$ electrons in total) was determined from the microwave cavity measurement. This measured mass value is in close agreement with that expected for a 320 μm diameter TESPEL pellet, *i.e.*, 18 μg. The difference in the pellet mass error bars is due to noise levels on the microwave signal. Next, the fraction of pellet particles deposited in the plasma is obtained by integrating the TS electron density profiles, before and after injection, over the plasma volume, assuming that electron density is flux-surface constant. A plasma volume of $2\pi R \times \pi a^2$ is considered, where the major radius, R, is 1.5 m is and the average plasma minor radius, a, is 0.1925 m. This is a reasonable approximation as pellet ablation occurs mainly inside $\rho = 0.7$, a radial position within which flux surfaces

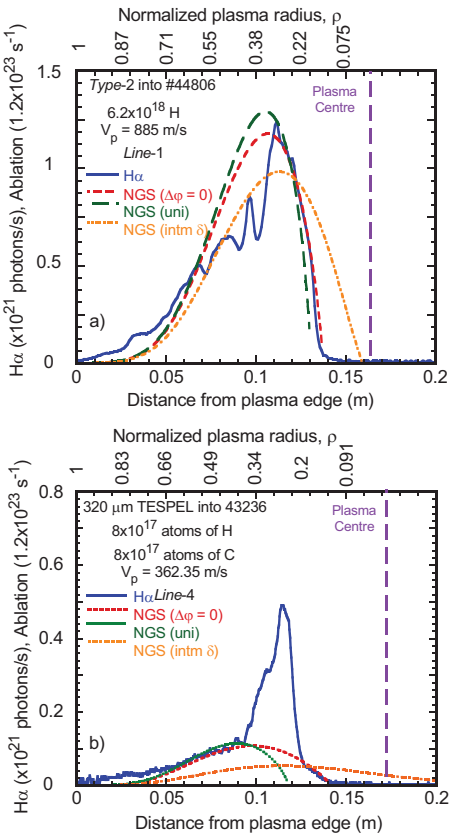

Fig. 4: (Colour online) Balmer H_α light emission profiles, obtained from TOP photodiode signals, for the distance into the plasma/normalized plasma radius for (a) Type-2 pellet injected along *Line*-1 and (b) 320 μm diameter unloaded TESPL injected along *Line*-4. In both cases the plasma is created and heated using ECRH and the target plasma line-averaged electron density is $\sim 4.2 \times 10^{18}$ m^{-3}. Also shown are ablation rates estimated using scaling laws where ($\Delta\varphi = 0$) is eq. (1) (red dashed line), (uni) is eq. (2) (green dotted line) and (intm δ) is eq. (3) (orange dot-dashed line) with H atom/s for (a) and CH molecule/s for (b). Also, ρ is normalized plasma radius, *i.e.*, $\rho = r/a$, a being the plasma minor radius.

tend towards being circular [21]. When compared with a rigorous integration that considers flux surface shapes, the resultant error is small, *i.e.*, no more than a few percent. As a cross calibration check, the line-averaged density is estimated from a pre-injection TS electron density profile and compared with the corresponding measured microwave interferometer value.

Experimental findings. In order to facilitate these studies, injections with both pellet types into similar target plasmas have been selected. In the case of TESPEL, only a few injections could be made with unloaded pellets into plasmas created with the standard configuration due to a limited number of experiment days on TJ-II and to the priority being given to impurity-loaded pellet injections. Thus, a cryogenic pellet injection, with a similar penetration depth to a successful TESPEL injection, has been selected in order to make comparative studies (see fig. 4). By successful, the authors consider that an

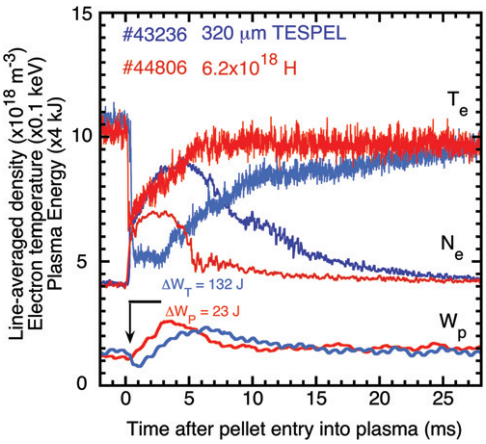

Fig. 5: (Colour online) Temporal evolution of the line-averaged electron density, core electron temperature ($\rho = 0.16$), and stored plasma energy before and after injection of a hydrogen pellet (6.2×10^{18} H) and a 320 μm diameter TESPEL pellet (unloaded) into similar discharges, #44806 (red) and #43236 (blue), respectively. The discharges were created and heated using ECRH.

unbroken TESPEL is deposited in the plasma (as determined from the microwave cavity and TOP signal). From fig. 4, the penetration depth is considered as the distance from the plasma edge at which the H_α signal returns to zero, *i.e.*, it has been determined experimentally that, in ECRH plasmas, pellets are accelerated neither radially nor toroidally [26].

For the same discharges, the evolution of the main plasma parameters, before and after the injections, is plotted in fig. 5. In the first instance, for line-averaged electron density, N_e, it is seen that after an initial abrupt jump in N_e just after an injection, its evolution is significantly slower after the TESPEL injection, while the relative increase in plasma density is significantly higher for the same. This latter point is confirmed by TS profiles recorded after pellet entry (see fig. 6). Furthermore, after analysis, it is determined that the fractions of pellet electrons deposited in the plasma core a few milliseconds after injection are $\sim 27 \pm 10\%$ for the cryogenic pellet and $\sim 80 \pm 5\%$ for TESPEL. Note: the larger error bars for the former arise from largest uncertainties in determining cryogenic pellet mass using the microwave cavity diagnostic [20]. Indeed, from refs. [21,27], the efficiency for cryogenic pellets is always $\leq 40\%$ for injections into ECRH plasmas in TJ-II. Hence, the $\geq \times 2$ increase in deposited pellet electron population observed for TESPEL pellets needs to be understood, more so given that values closer to 100% were obtained for some tracer-loaded pellet injections (made under different target plasma conditions). Moreover, in the same figure, it is observed that the cryogenic pellet electron deposition profile is rather flat while, for TESPEL, it peaks close to the plasma centre.

Discussion. – *Penetration depth.* H_α radial emission profiles are presented in fig. 4 for the two pellet types injected into similar target plasmas. Although their H_α

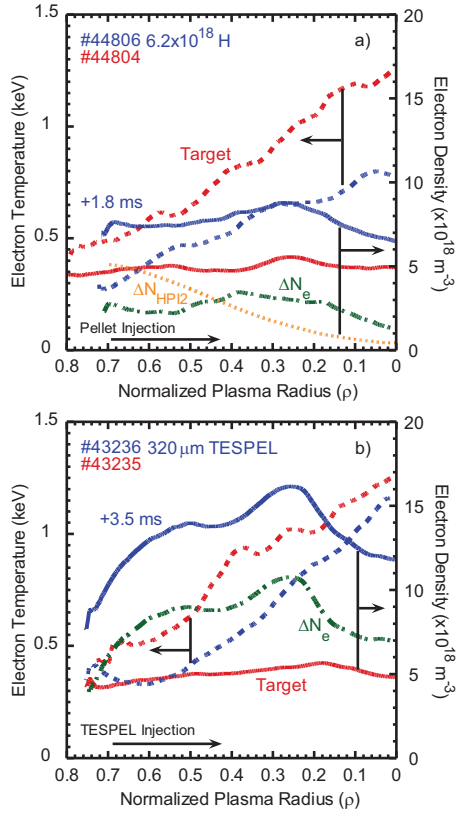

Fig. 6: (Colour online) Thomson scattering electron temperature (dashed) and density (continuous) profiles obtained before (Target, red) and several milliseconds after the injection (blue) of (a) a solid hydrogen pellet injected along *Line*-1, and (b) a 320 μm diameter TESPEL injected along *Line*-4. For both cases, plasma is created and maintained by ECRH and the target plasma line-averaged electron density is $\sim 4.2\times10^{18}$ m^{-3}. δN_e (green) is the difference between pre- and post-injection density profiles. HPI2 (orange) is the deposition profile, simulated using the HPI2 code, for the cryogenic pellet.

emissions profiles do not directly reflect ablation, the profiles allow penetration depths to be established for comparison with scalings. Before proceeding to discuss this it should be noted that, in fig. 4(b), the large jump in the H_α emission near the end of the ablation process can be attributed to the enhanced light emission stimulated by a small population of suprathermal electrons residing in the plasma core, between $\rho = 0.2$ and 0.34 in these off-axis heated plasmas, and/or to light emission associated with back drifting plasmoid [26]. Some enhanced light emission may also be present in the H_α profile of fig. 4(a). However, the contribution of this small population to overall pellet ablation is considered minor [26]. An edge suprathermal electron population, which would be more critical for ablation rates, is not observed in these profiles.

Ablation rate curves, determined using three simple analytic formulas (scalings) [17], are also plotted in fig. 4. The first scaling considered, from eq. (20) of [17], reflects strong NGS while assuming no potential drop, $\Delta\phi = 0$, at the neutral cloud/surrounding plasma boundary, NGS($\Delta\phi = 0$). Strong signifies that cloud shielding is dominant, *i.e.*, $\delta \ll 1$, where δ, the shielding factor, is the ratio of heat flux passing through the cloud and reaching the pellet surface to the primary heat flux in the surrounding plasma. This scaling, with pellet-type parameters included, gives the ablation rate (particles/s) as

$$N_1(\text{particle/s}) = 1.94\times10^{14}\cdot N_e^{0.45}\,(\text{cm}^{-3})\cdot T_e^{1.72}\,(\text{eV}) \cdot r_\text{p}^{1.44}\,(\text{cm})\cdot\varepsilon^{-0.16}\,(\text{eV})\cdot A_\text{p}^{-0.28}\,(\text{amu})\cdot Z_\text{p}^{-0.56}\cdot(\gamma-1)^{0.28}. \quad (1)$$

Here N_e and T_e are the local electron density and temperature, respectively, r_p is the pellet radius, ε is the sublimation energy, A_p is the atomic mass, Z_p is the nuclear charge number and γ is gas adiabatic index. For hydrogen, $\varepsilon = 0.0053$ eV, $A_\text{p} = 1$, $Z_\text{p} = 1$, and $\gamma = 7/5$, while for CH molecules, $\varepsilon = 0.0625$ eV, $A_\text{p} = 6.5$, $Z_\text{p} = 3.5$, and $\gamma = 8/6$ [17]. The second scaling, eq. (15) of [17], is a unified strong NGS scaling law designed for any pellet material, NGS(uni). It is given by

$$N_2(\text{particle/s}) = 4\times10^{15} N_\text{e}^{0.33}\,(\text{cm}^{-3})\cdot T_\text{e}^{1.83}\,(\text{eV})\cdot \cdot r_\text{p}^{1.33}\,(\text{cm})\cdot A_\text{p}^{-0.33}\,(\text{amu})\cdot Z_\text{p}^{-0.66}. \quad (2)$$

Finally, the third scaling considered, NGS(intm δ), is eq. (25) of [17]. It uses the mean of two limiting cases, *i.e.*, $\delta \to 0$ and $\delta \to 1$, and is estimated as

$$N_3(\text{particle/s}) = N_1\cdot N_4/(N_1+N_4). \quad (3)$$

Here N_1 is eq. (1) while N_4, eq. (26) of [17], assumes a completely unshielded electron heat flux with $\delta = 1$ and is given by

$$N_4 = 5.25\times10^{15}\cdot N_\text{e}\,(\text{cm}^{-3})\cdot T_\text{e}^{1.5}\,(\text{eV})\cdot r_\text{p}^2\,(\text{cm})/\varepsilon\,(\text{eV}). \quad (4)$$

Here, eq. (4) is similar to the scaling developed by Khlopenkov and Sudo for TESPEL [16], albeit a fixed ε value was not used therein, rather a range of values was considered.

When these scalings are applied for H and C_8H_8 pellets into the TJ-II target plasmas of interest, it is found that penetration depths are best predicted by scaling N_1 for both types, although for the H pellet the scaling N_2 also gives good agreement. In contrast, for both pellets, N_3 predicts significantly deeper penetrations. This coincides with ref. [17] when the authors studied a C_8H_8 pellet injection into the stellarator LHD, *i.e.*, the N_1 model provided the most reliable prediction of penetration depth while eq. (3) significantly overestimated the same. These findings provide additional confidence for use of the latter scaling for other devices, for instance for the planned TESPEL system on the stellarator W7-X [10].

Particle deposition. The observations in figs. 5 and 6, showing plasma evolution and pellet material deposition, can be understood by considering several physics aspects that occur during and after an injection. In the first instance, complete cryogenic pellet ablation occurs within

150 μs after pellet entry into the plasma. Hydrogen atoms in the plasmoid that surrounds the cryogenic pellet become ionized rapidly (the ionization time is $\sim$6.7 μs for plasma electron density and temperature of $5 \times 10^{18}\,\mathrm{m}^{-3}$ and 500 eV, respectively) [28]. Subsequently, rapid outwards acceleration and deceleration of this plasmoid occurs (this will be discussed in more detail later). The ionized particles that remain in the plasma diffuse more slowly around the plasma volume, *i.e.*, complete particle distribution, which is reflected in part by the line-averaged density, is achieved within a couple of milliseconds in the TJ-II [21]. Next, the electron density shows an approximated exponential decay back to the pre-injection level. In parallel, plasma cooling during and after injection occurs due to ablation, dissociation and ionization processes (36.4 eV loss per ion pair [29]) plus the addition of cold electrons to the plasma. Indeed, the initial plasma stored energy loss (E_L) of 23 ± 10 J due to the injection, as measured with a diamagnetic loop [14], agrees well with the predicted loss, 18 J, where $E_\mathrm{L}\,(\mathrm{J}) = (N_\mathrm{H}/2) \times 36.4 \times 1.6 \times 10^{-19}$. It is assumed that radiation losses are $<$ 1 eV/H atom [21].

In contrast, complete TESPEL pellet ablation requires $\geq 300\,\mu$s during which the polystyrene molecules undergo an initial ionization process (8.4 eV per C_8H_8), multiple dissociations (assuming 4.3 eV, 3.6 eV and 6.3 eV per C-H, C-C and C=C bonds, respectively [30]) plus subsequent ionizations. For the latter, the first ionization of carbon (11.3 eV/C atom) occurs in $\sim$1.7 μs while further ionizations (24.4, 47.9, 64.5, 392 and 490 eV/C ion) to higher states, *i.e.*, C^{+2} through to C^{+6}, require $\sim$6.7 μs, $\sim$22 μs, $\sim$67 μs, $\sim$0.9 ms, and $\sim$3.3 ms, respectively [28]. Hence, the initial rapid jump in plasma line-averaged density of fig. 5 is followed by a slow rise to density maximum, $\sim$5 ms. Moreover, these multiple processes result in a much larger plasma stored energy drop, 132 ± 20 J. A simple summation of all of these processes, in which carbon ionization dominates, predicts a 137 J stored energy loss.

The differences between the post-injection line-averaged electron densities of fig. 5 and the electron density profiles of fig. 6 can be understood by considering the previously inferred $E \times B$ induced acceleration of the partially ionized plasmoid that surrounds an ablating pellet [2]. The development of this drift is used to explain the well-known outward displacement of pellet material in magnetically confined plasma devices, in particular for LFS injections of hydrogen pellets [2,21]. It arises due to the interaction between the background magnetic field, B_∞, and an electric field, E, that results from charge separation across the plasmoid. During the initial short drift phase, acceleration of the plasmoid, in opposite directions for electrons and ions, is induced. The time evolution of its drift velocity can be written, for non-axisymmetric devices, as $\delta V_\mathrm{d}/\delta t = -2(p_0 - p_\infty)\nabla_\perp B_\infty / n_0 m_\mathrm{i} B_\infty$ [31], where p is the pressure, n is the density, m_i is the ion mass, and the subscripts 0 and ∞ refer to cloud and background plasma, respectively. For the TJ-II, the cross-field gradient scale-length, $L_\mathrm{B} = B_\infty/\nabla_\perp B_\infty$, is close to $1\,\mathrm{m}^{-1}$ on the LFS of the plasma centre, thus V_d is directed towards the plasma outer edge (see fig. 3). It should be noted that L_B is much larger than $1/R$, hence the drift in TJ-II will be large compared to an equivalent aspect ratio tokamak (see fig. 3). In contrast, several mechanisms lead to deceleration of the pellet cloud motion [2]. It is considered that the most efficient for non-axisymmetric devices is Rozhansky's effect. It is accounted for by adding the drift-dampening factor, $A[L_0]$, to the $\delta V_\mathrm{d}/\delta t$ term [31,32]. The combined PI/TESPEL experimental set-up means that the cross-field gradient scale-lengths, $L_\mathrm{B} = B_\infty/\nabla_\perp B_\infty$, are almost identical for flight paths through the plasma. Thus, assuming that the background plasma and cloud pressures are equal, or similar, for both, and that $A[L_0]$ is independent of the pellet type [31], then the ion mass ($m_\mathrm{i} = 1$ amu for a hydrogen atom and 12 amu for a carbon atom) is the only parameter that can explain differences in plasmoid drift and hence deposition profiles and efficiency. Hence, this significantly larger TESPEL ion mass during the initial stage of plasmoid acceleration may explain both the significant difference in deposited pellet electrons and the radial positions of the deposition profiles.

Plasmoid drift is considered in the Hydrogen Pellet Injection code, HPI2, which was recently adapted for TJ-II [26,33]. A simulation, made using the TJ-II version, for a LFS injection of a cryogenic pellet generates an electron deposition profile, ΔN_HPI2, which is similar in magnitude to the difference between the pre- and post-injection electron density profiles, ΔN_e, of fig. 6. It should be noted that post-ablation radial transport is not considered in the model. However, the higher core ΔN_e in fig. 6, with respect to ΔN_HPI2, is explained in a previous work on TJ-II in which it is described how core ΔN_e evolves for several milliseconds (5 to 6 ms) after particle deposition, *i.e.*, core and edge electron densities rise and fall, respectively [21], this evolution being due to a partial inward transport of pellet electrons [26]. In contrast, the particle confinement time for TJ-II plasmas is between 5 and 15 ms, being $\sim 10 \pm 3$ ms when the line-averaged density goes above a critical density, *i.e.*, $\sim 6 \times 10^{18}\,\mathrm{m}^{-3}$, for ECRH [34,35].

A similar simulation cannot be made at present for TESPEL pellets as HPI2 is not prepared for heavier atomic elements or complicated molecules. However, simple calculations can be made, based on HPI2 results for hydrogen, to obtain a prediction for the fraction of TESPEL particles that remain within the last closed flux surface (LCFS). In the cryogenic case, average outwards radial drift velocities and drift times are obtained for H clouds originating at different radial positions, ρ, along the pellet flight path [26]. These range from 380 to $\sim$1200 m/s for plasmoids originating from ρ between 0.85 and 0.3, respectively, while increasing rapidly inside $\rho = 0.3$ to reach $\sim$12 km/s at $\rho = 0.17$. From the same H simulation, by considering only those plasmoids that remain within the plasma, *i.e.*, material ablated between $0.5 \geq \rho \geq 0.22$, an upper limit of $\sim$140 μs for radial drift time is established.

Next, returning to TESPEL and assuming that C_8H_8 molecules dissociate to H and C ions, as a first approximation it is reasonable to suppose that H should achieve radial drift velocities as above while, from the mass scaling in $\delta V_\mathrm{d}/\delta t$, C should reach average velocities that are 12 times lower (friction between the two species is not considered). Hence, for a 140 μs drift time limit, no C ions should reach the LCFS since $V_\mathrm{d}(\rho) \times 140\,\mu$s is shorter than the plasmoid origin to LCFS distances, *e.g.*, this is 0.08 m for $\rho = 0.2$, where $V_\mathrm{d}(\rho) = 6900/12$ m/s. In such a situation, all the C plus 27% of the H (from the cryogenic case) should contribute to deposition, *i.e.*, $6/7 + 0.27/7 \times 100\% = 89.6\%$. This is in reasonable agreement with the experimental value obtained for the 320 μm TESPEL pellet, $\sim 80 \pm 5\%$, given the simplicity of the model. However, because of the large differences in H and C drift velocities, it is reasonable to consider that their clouds should separate thereby resulting in lower plasmoid pressures, p_0, and hence reduced $\delta V_\mathrm{d}/\delta t$.

The findings reported here have several implications for pellet injection experiments in magnetically confined plasma devices. In the first instance they highlight the importance of considering the pellet electron content when designing TESPEL, or other solid pellet, injection experiments for plasma devices. Such considerations should also be considered for impurity transport experiments made using pellets since nearly 100% of the tracer population may be deposited within the LCFS of the plasma. The findings may also have implications for dust injection experiments on such devices, in particular for heavy-Z elements. Finally, in the future TESPEL experiments it would be to informative to view ablating TESPEL pellets with a fast-frame camera simultaneously equipped with bandpass filters centred on H and C emission lines in order to study the radial drifting of the H and C clouds.

* * *

This work has been carried out within the framework of the EUROfusion Consortium and has received funding from the Euratom research and training programme 2014–2018 under grant agreement No. 633053. The views and opinions expressed herein do not necessarily reflect those of the European Commission. In addition, it is partially financed by grants from the Spanish Ministerio de Economía y Competitividad (Refs. ENE2013-48679-R) and by NIFS/NINS under the project of Formation of International Scientific Base and Network (KEIN1102 and KEIN1104) and Young Researchers Supporting Program (UFEX106).

Published under license from EURATOM.

REFERENCES

[1] Milora S. L. *et al.*, *Nucl. Fusion*, **35** (1995) 657.
[2] Pégourié B., *Plasma Phys. Control. Fusion*, **49** (2007) R87.
[3] Spitzer L., Grove D. J., Johnson W. E., Tonks L. and Westendorp W. F., *Problems of the Stellarator as a Useful Power Source*, USAEC Report NYO-6047 (1954), unpublished.
[4] Baylor L. R. *et al.*, *Nucl. Fusion*, **47** (2007) 443.
[5] Ledl L. *et al.*, *Nucl. Fusion*, **44** (2004) 600.
[6] Smirnov R. D. *et al.*, *Contrib. Plasma Phys.*, **52** (2012) 435.
[7] Sudo S., *J. Plasma Fusion Res.*, **69** (1993) 1349.
[8] Sudo S. *et al.*, *Plasma Fusion Res.*, **9** (2014) 1402039.
[9] Sakamoto R. *et al.*, *Nucl. Fusion*, **46** (2006) 884.
[10] Thomsen H. *et al.*, *J. Instrum.*, **10** (2015) P10015.
[11] Dibon M. *et al.*, *Fusion Eng. Des.*, **98-99** (2015) 1759.
[12] Sánchez J. *et al.*, *Nucl. Fusion*, **55** (2015) 104014.
[13] Tamura N. *et al.*, *Rev. Sci. Instrum.*, **87** (2016) 11D619.
[14] McCarthy K. J., in *Diagnostic tools for probing hot magnetically confined plasmas, XXXIII Reunión Bienal de la Real Sociedad Española de Física: 21er Encuentro Ibérico para la Enseñanza de la Física*, Vol. **IV** (PUBliCan, ediciones de la Universidad de Cantabria, Santander, Spain) 2011, p. 65, ISBN 978-84-86116-40-8.
[15] Kuteev B., *Nucl. Fusion*, **35** (1995) 431.
[16] Khlopenkov K. and Sudo S., *Rev. Sci. Instrum.*, **69** (1998) 3194.
[17] Sergeev V. Yu. *et al.*, *Plasma Phys. Rep.*, **32** (2006) 363.
[18] Fontdecaba J. M. *et al.*, *Rev. Sci. Instrum.*, **85** (2014) 11E803.
[19] McCarthy K. J. *et al.*, *PoS(ECPD 2015)* (2015) 134.
[20] Combs S. K. *et al.*, *Fusion Sci. Technol.*, **64** (2013) 513.
[21] McCarthy K. J. *et al.*, *Nucl. Fusion*, **57** (2017) 056039.
[22] Tamura N. *et al.*, *Plasma Fusion Res.*, **10** (2015) 1402056.
[23] McNeill D. H., *J. Nucl. Mater.*, **162** (1989) 476.
[24] Herranz J. *et al.*, *Fusion Eng. Des.*, **65** (2003) 525.
[25] `http://polymerdatabase.com/polymers/polystyrene.html.`
[26] Panadero N. *et al.*, to be published in *Nucl. Fusion.*
[27] Velasco J. L. *et al.*, *Plasma Phys. Control. Fusion*, **58** (2016) 084004.
[28] Kato T., Masai K. and Arnaud M., NIFS Research Report NIFS-DATA-14 (Nagoya, Japan), available at: `www.nifs.ac.jp/report/nifs-data014.html.`
[29] Febler F. S. *et al.*, *Nucl. Fusion*, **19** (1979) 1061.
[30] Lide D. R., *CRC Handbook of Chemistry and Physics*, 72nd edition (CRC Press Incorporated, Boca Raton) 1991–1992.
[31] Matsuyama A. *et al.*, *Plasma Fusion Res. Lett.*, **7** (2012) 1303006.
[32] Rozhansky V. A. *et al.*, *Plasma Phys. Control. Fusion*, **46** (2004) 575.
[33] Koechel F. *et al.*, *Modelling of Pellet Particle Ablation and Deposition: The Hydrogen Pellet Injection Code HPI2*, EUROfusion Preprint EFDA-JET-PR(12)57.
[34] Tabarés F. L. *et al.*, *Plasma Phys. Control. Fusion*, **43** (2001) 1023.
[35] Tallents S. *et al.*, *Plasma Phys. Control. Fusion*, **56** (2014) 075024.